

Ultrafast Manipulation of Spin Dynamics in Time-Resolved Raman Scattering

Yao Wang,¹ Thomas P. Devereaux,^{2,3} and Cheng-Chien Chen⁴

¹*Department of Physics, Harvard University, Cambridge, Massachusetts 02138, USA*

²*SLAC National Accelerator Laboratory, Stanford Institute for Materials and Energy Sciences,
2575 Sand Hill Road, Menlo Park, California 94025, USA*

³*Geballe Laboratory for Advanced Materials, Stanford University, California 94305, USA*

⁴*Department of Physics, University of Alabama at Birmingham, Birmingham, Alabama 35294, USA*

(Dated: April 19, 2019)

Ultrafast characterization and control of spin interaction are critical to understanding and manipulating emergent phenomena in strongly correlated systems. To address this question, we use exact diagonalization to simulate the single-band Hubbard model in a pump-probe experiment. Different ultrafast processes are shown to exist in the time-resolved B_{1g} Raman spectra and dominate under different pump conditions. For high-frequency and off-resonance pumps, we show that the Floquet theory works well in capturing the softening of bimagnon excitation. By comparing the Stokes/anti-Stokes spectra, we also show that effective heating dominates at small pump fluences, while coherent many-body effect starts to take over at larger pump amplitudes especially at frequencies on-resonance to the Mott gap. Time-resolved Raman scattering thereby provides the platform to explore different ultrafast processes and design material properties out of equilibrium.

PACS numbers: 78.47.J-, 42.65.Dr, 78.47.da, 72.10.Di

Ultrafast control of physical properties is an ultimate goal of nonequilibrium studies[1, 2]. Among different degrees of freedom in solids, spin physics plays an important role in unconventional superconductivity[3–5], frustrated magnetism[6, 7], magnetic materials[8], and spintronics[9, 10]. Understanding collective spin excitations out of equilibrium is also crucial for the explanation of photoinduced emergent phenomena like transient superconductivity[11–13]. Due to the fluence limitation, however, the spin-sensitive inelastic neutron scattering cannot be applied as an ultrafast technique. Therefore, although nonequilibrium dynamical spin structure factors were predicted theoretically[13–16], they cannot be directly measured in ultrafast experiments. With recent advance of photon spectroscopies, probing nonequilibrium spin dynamics through charge channel becomes promising[17]. For example, Raman scattering was used to measure bimagnon excitation and provide information for the underlying spin interaction[18–21]. Time-resolved Raman scattering was employed to study lattice and molecule vibrations[22–29], as well as collective excitations of quantum materials in recent years[17, 30]. As we shall demonstrate theoretically below, time-resolved Raman spectroscopy also can be a powerful tool to probe and manipulate spin interaction out of equilibrium.

On general ground, pump-induced ultrafast behaviors include effective heating, transient Floquet band renormalization, and non-thermal many-body excitation. These processes are sketched in Fig. 1. Under an infinite long periodic driving field, a system is known to exhibit a superposition of Floquet steady states[31, 32]. Via photo-assisted virtual hoppings, the corresponding band renormalization and replicas can correct the effective spin exchange J [15, 33]. However, this process requires infinitely long pump and off resonance in regard to the

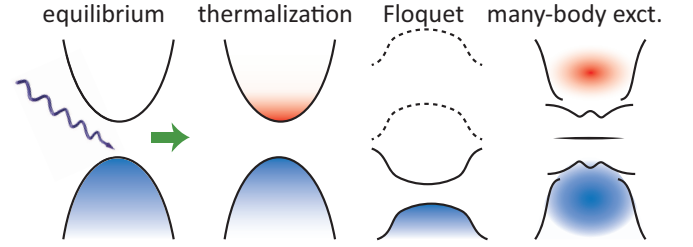


FIG. 1: Different ultrafast processes induced by a pump field: effective heating or thermalization, transient (Floquet) band renormalization, and non-thermal many-body excitation.

charge gap, which is not practical in reality. A resonant excitation is unavoidable due to existence of higher-energy unoccupied states. This partial resonance to the lowest order can cause effective heating[34–36], unless the systems is integrable or many-body localized as in ideal theoretical scenarios[37–39]. Reducing the pump width and probe delay can suppress thermalization[40–42], but meanwhile restrict exotic Floquet physics. Moreover, many-body physics can lead to nonlinear modulation of electronic structure, which cannot be attributed simply to effective heating[43–45]. The above three effects exist in realistic ultrafast experiments, and their interplay determines the final Raman spectra in the time domain.

In this Letter, we perform exact diagonalization on a square-lattice single-band Hubbard model to study time-resolved Raman scattering, in order to understand how different ultrafast processes compete and compromise during a pump field. We show that bimagnon excitations can be reflected in Raman spectra, and that each mechanism depicted in Fig. 1 can become dominant under different pump conditions. In particular, a low-frequency resonant pump results in clear thermalization, while a

high-frequency nonresonant pump causes Floquet renormalization of energy scale J . Both scenarios however are violated under extremely strong pumps, where many-body excitations take over. Being the first theoretical investigation of time-resolved Raman scattering, our work provides a platform to study different ultrafast mechanisms and nonequilibrium spin excitations.

We first review the theory of Raman scattering. The influence of an electromagnetic field can be introduced through a Peierls substitution $c_{i\sigma} \rightarrow c_{i\sigma} e^{-i \int_{-\infty}^{\mathbf{r}_i} \mathbf{A}(\mathbf{r}', t) \cdot d\mathbf{r}'}$. Here, $c_{i\sigma}$ is a fermionic annihilation operator for electron of spin σ on lattice site \mathbf{i} , and \mathbf{A} is a vector potential. We use the natural unit to simplify mathematical notations. The Hamiltonian \mathcal{H} can be expanded in powers of the probe field $\mathbf{A}^{(\text{pr})}$:

$$\mathcal{H} \approx \mathcal{H}_0 - \sum_{\mathbf{r}, \alpha} \hat{j}_\alpha(\mathbf{r}) A_\alpha^{(\text{pr})}(\mathbf{r}, t) - \frac{1}{2} \sum_{\mathbf{r}, \alpha, \beta} \hat{\gamma}_{\alpha\beta}(\mathbf{r}) A_\alpha^{(\text{pr})}(\mathbf{r}, t) A_\beta^{(\text{pr})}(\mathbf{r}, t), \quad (1)$$

where $A_\alpha^{(\text{pr})}(\mathbf{r}, t) = \int_{\mathbf{r}}^{\mathbf{r}+\mathbf{1}_\alpha} \mathbf{A}^{(\text{pr})}(\mathbf{r}', t) \cdot d\mathbf{r}'$, and α denotes the light polarization direction. \hat{j}_α and $\hat{\gamma}_{\alpha\beta}$ are respectively the paramagnetic current density operator and scattering vertex. In the Fourier space of momentum transfer, $A_\alpha^{(\text{pr})}(\mathbf{q}, t) = \frac{1}{N} \sum_{\mathbf{r}} e^{-i\mathbf{q} \cdot \mathbf{r}} A_\alpha^{(\text{pr})}(\mathbf{r}, t)$, $\hat{j}_\alpha(\mathbf{q}) = \sum_{\mathbf{k}\sigma} (\partial \varepsilon_{\mathbf{k}} / \partial k_\alpha) c_{\mathbf{k}+\mathbf{q}/2, \sigma}^\dagger c_{\mathbf{k}-\mathbf{q}/2, \sigma}$, and $\hat{\gamma}_{\alpha\beta}(\mathbf{q}) = \sum_{\mathbf{k}\sigma} (\partial^2 \varepsilon_{\mathbf{k}} / \partial k_\alpha \partial k_\beta) c_{\mathbf{k}+\mathbf{q}/2, \sigma}^\dagger c_{\mathbf{k}-\mathbf{q}/2, \sigma}$. For nearest-neighbor (N.N.) hopping on square lattice, the band structure $\varepsilon_{\mathbf{k}}$ is $-2t_h(\cos k_x + \cos k_y)$.

While the single photon absorption ($\propto A_\alpha^{(\text{pr})}$) concerns measuring photocurrent in optical conductivity, Raman scattering as a photon-in-photon-out procedure ($\propto A_\alpha^{(\text{pr})} A_\beta^{(\text{pr})}$) probes particle-hole excitation with a form factor. The Raman cross section is proportional to the transition rate determined by Fermi's golden rule:

$$\mathcal{R}(\mathbf{q}, \omega_i, \omega_s) = \sum_n \left| \langle n | \hat{M}(\mathbf{q}, \omega_i, \omega_s) | G \rangle \right|^2 \delta(\omega + E_G - E_n), \quad (2)$$

where $|G\rangle$ and $|n\rangle$ are respectively the ground and excited states, and $\omega = \omega_i - \omega_s$ is the photon energy loss.

The effective light-scattering operator $\hat{M}(\mathbf{q}, \omega_i, \omega_s)$ contains the following two-photon processes:

$$\sum_{\alpha, \beta} \hat{\mathbf{e}}_\alpha^{(i)} \hat{\mathbf{e}}_\beta^{(s)} \left[\hat{\gamma}_{\alpha\beta} - \hat{j}_\beta \frac{1}{\bar{\mathcal{H}} - \omega_i} \hat{j}_\alpha + \hat{j}_\alpha \frac{1}{\bar{\mathcal{H}} + \omega_s} \hat{j}_\beta \right]. \quad (3)$$

Here, $\bar{\mathcal{H}} \equiv \mathcal{H} - E_G$ when \hat{M} acts on the ground state, and $\hat{j}_{\alpha/\beta}$ is implicitly associated with momentum transfer $\mathbf{q}_{i/s}$. Note that the last two terms in Eq. (3) involve virtual processes through resonant intermediate states. The nonresonant Raman scattering is determined by the first term in Eq. (3). In this sense, $\hat{M}(\mathbf{q}, \omega_i, \omega_s)$ describes a collective excitation with direct energy ω and

momentum \mathbf{q} transfers between electrons and photons. The resulting nonresonant Raman response then reads

$$\mathcal{R}_N(\mathbf{q}, \omega) = \frac{1}{\pi} \text{Im} \left\langle G \left| \hat{\gamma}^\dagger(\mathbf{q}) \frac{1}{\bar{\mathcal{H}} - E_G - \omega - i\delta} \hat{\gamma}(\mathbf{q}) \right| G \right\rangle, \quad (4)$$

where $\hat{\gamma}(\mathbf{q}) = \sum_{\alpha, \beta} \hat{\mathbf{e}}_\alpha^{(i)} \hat{\gamma}_{\alpha\beta}(\mathbf{q}) \hat{\mathbf{e}}_\beta^{(s)}$, and δ is a lifetime broadening effect. Below we focus on the long-wavelength limit $\mathbf{q} = \mathbf{q}_i - \mathbf{q}_s \approx 0$ and omit the \mathbf{q} label.

On square lattice, the scattering vertices can be decomposed in the irreducible representation of D_{4h} point group[20]. Specifically, in the $B_{1g}(xx - yy)$ channel

$$\hat{\gamma}_{B_{1g}} = \sum_{\mathbf{k}\sigma} \left(\frac{\partial^2}{\partial k_x^2} - \frac{\partial^2}{\partial k_y^2} \right) \varepsilon_{\mathbf{k}} c_{\mathbf{k}, \sigma}^\dagger c_{\mathbf{k}, \sigma}. \quad (5)$$

On square lattice with N.N. hopping, the vertex in the brackets is proportional to $(\cos k_x - \cos k_y)$.

The theory of Raman scattering can be extended to nonequilibrium, and a detailed derivation is given in the Supplementary Material[46]. The resulting time-resolved nonresonant optical Raman cross section reads

$$R_{B_{1g}}(\omega, t) = \iint dt_1 dt_2 e^{i\omega(t_2 - t_1)} g(t_1; t) g(t_2; t) \chi(t_1, t_2). \quad (6)$$

Here, $\chi(t_1, t_2) = i \langle \psi(t_2) | \hat{\gamma}_{B_{1g}}(t_2) \mathcal{U}(t_2, t_1) \hat{\gamma}_{B_{1g}}(t_1) | \psi(t_1) \rangle$, and \mathcal{U} is the time propagator. In the interaction picture,

$$\hat{\gamma}_{B_{1g}}(t) = t_h \sum_{\mathbf{k}} [\cos(k_x - A_x(t)) - \cos(k_y - A_y(t))] n_{\mathbf{k}}. \quad (7)$$

Note that $\mathbf{A}(t)$ is the pump (instead of the probe) field. The probe shape function $g(t'; t)$ can be approximated by a gaussian pulse centered at t with time width σ_{pr} . When the pump fluence vanishes and the system becomes time-translationally invariant, Eq. (6) reproduces the equilibrium Raman cross section with a gaussian linewidth $\sim 1/(\sqrt{2}\sigma_{\text{pr}})$ [46].

With the above formula, below we use exact diagonalization to compute the time-resolved Raman spectra on the single-band Hubbard model:

$$\mathcal{H} = -t_h \sum_{\langle \mathbf{i}, \mathbf{j} \rangle, \sigma} c_{i\sigma}^\dagger c_{j\sigma} + U \sum_{\mathbf{i}} n_{i\uparrow} n_{i\downarrow}. \quad (8)$$

The Hubbard interaction is set to $U = 8t_h$ as a typical choice for high- T_c cuprate materials. This choice leads to an effective spin exchange energy $J = 4t_h^2/U = 0.5t_h$. The calculation is performed on a Betts 12A cluster[46]. The parallel Arnoldi method[47, 48] is used to determine the equilibrium ground state wavefunction $|\psi(t = -\infty)\rangle$.

While the probe field $\mathbf{A}^{(\text{pr})}$ is treated with perturbation theory, the pump field $\mathbf{A}(t)$ is considered explicitly through a Peierls substitution. Here we use an oscillatory gaussian vector potential in the temporal gauge to simulate a pulsed laser pump:

$$\mathbf{A}(t) = A_0 e^{-t^2/2\sigma^2} \cos(\Omega t) \mathbf{e}_{\text{pol}}, \quad (9)$$

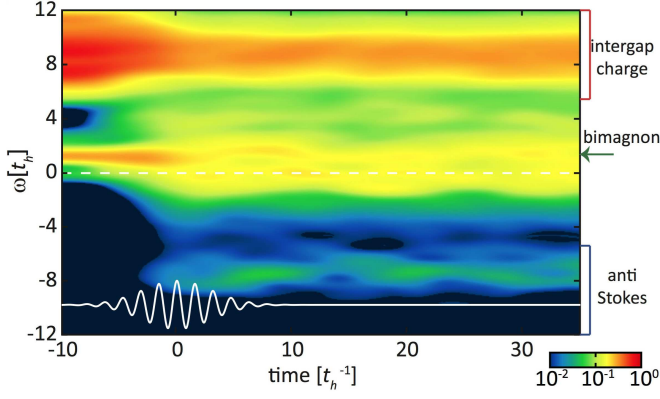


FIG. 2: Time-resolved B_{1g} Raman spectra with pump polarization $\mathbf{e}_{\text{pol}} = \mathbf{e}_x$, frequency $\Omega = 4t_h$, and amplitude $A_0 = 0.6$. The bimagnon and Stokes/anti-Stokes charge excitations are marked on the right to guide the eye. Energy zero (defined as the equilibrium ground state energy) is denoted by the dashed white line. The oscillatory gaussian pump is drawn as a solid white curve.

where A_0 , σ , and Ω are respectively the pump amplitude, width, and frequency. The time $t = 0$ corresponds to the center of the pump. Note that due to the tilted geometry of the 12A cluster, the diagonal polarization in momentum space in fact reflects the horizontal polarization in real space[46]. We use the Krylov subspace technique[49, 50] to evaluate the time evolution of the wavefunction $|\psi(t+\delta t)\rangle = e^{-i\mathcal{H}(t)\delta t}|\psi(t)\rangle$.

Figure 2 shows the time-resolved B_{1g} Raman spectra with the horizontal pump polarization $\mathbf{e}_{\text{pol}} = \mathbf{e}_x$. Before the pump enters, the equilibrium spectrum exhibits a low-energy peak at $\sim 1.3t_h$ attributed to bimagnon excitation. In the strong coupling limit $U \rightarrow \infty$, the bimagnon energy $\sim 3J$ is renormalized from $4J$ (two times the single magnon bandwidth), representing two locally bounded spin-flip excitations. Further calculations with different strengths of U have supported the assignment of the low-energy bimagnon peak[46]. In addition, a cloud of cross-gap charge excitations exist above the Mott gap energy $\sim U - 4t_h$. With our current choice of U , these charge modes are well-separated from the bimagnon peak, which thereby provides an opportunity to track these excitations individually. Since the 12A cluster breaks C_4 symmetry, the ground state shows a small, unphysical elastic peak[46]. No signals are observed below zero energy, as the system is at the ground state.

In the presence of pump, the bimagnon energy softens transiently and becomes indistinguishable from the elastic peak. This can be attributed to a renormalized spin exchange interaction through the Floquet photo-assisted process, as discussed later in Eqs. (10) and (11). Meanwhile, the anti-Stokes features start to appear with the pump, and the Stokes excitations across the Mott gap are suppressed accordingly. This is a signature of pump-induced thermalization. Moreover, the energies

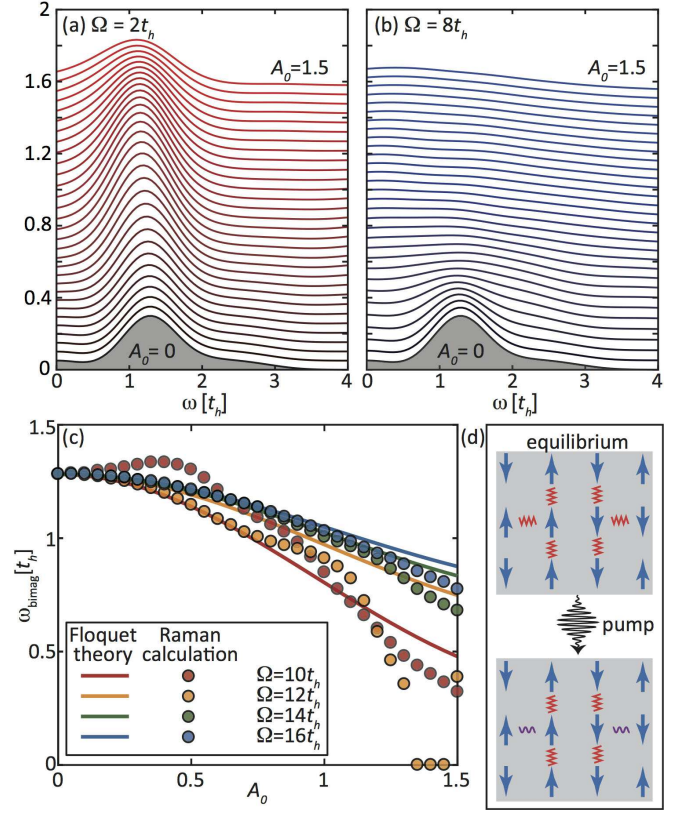


FIG. 3: The EDC curves for B_{1g} Raman spectra with pump amplitude A_0 varying from 0 (bottom) to 1.5 (top) at pump frequency (a) $\Omega = 2t_h$ and (b) $\Omega = 8t_h$. The time is fixed at $t = 0$ (the center of the pump). (c) Bimagnon energies as a function of A_0 under high-frequency pumps ($\Omega > U$). The solid curves are predicted by the Floquet theory in the nonresonant limit. (d) Schematic cartoon showing specific spin exchange bonds altered by a pump pulse field.

of cross-gap excitations are modified by the pump, and new spectral poles near $4t_h$ start to develop. These new “in-gap” states indicate the appearance of many-body excitations beyond a simple heating effect. As mentioned before, the three ultrafast processes in Fig. 1 are all reflected in the time-resolved Raman spectra.

Due to both thermalization and many-body scattering, the bimagnon excitation can become less well-defined. Figure 3 tracks the energy distribution curve (EDC) for the bimagnon peak at time $t = 0$ under various pump profiles. At a small pump frequency $\Omega = 2t_h$ [Fig. 3(a)], the bimagnon energy remains unchanged, but its peak width is gradually broadened with increasing pump amplitude. This is consistent with the thermalization mechanism, where a small amount of particle-hole excitations are created across the Mott gap. On the other hand, at a larger pump frequency $\Omega = 8t_h$ [Fig. 3(b)], the bimagnon energy and width can strongly depend on the pump amplitude. The non-thermal mechanisms underlying these changes are discussed below.

As shown in Fig. 3(c) for $\Omega = 12t_h - 16t_h$, a high-frequency pump with strong amplitude can soften significantly the spin exchange J or the bimagnon energy[51]. This behavior can be understood by the Floquet renormalization at the nonresonant limit ($m\Omega \neq U$)[15]:

$$\frac{J(A_0)}{J(A_0=0)} = \sum_{m=-\infty}^{+\infty} \frac{\mathcal{J}_m(A_0)^2}{1 + m\Omega/U}, \quad (10)$$

in which $\mathcal{J}_m(x)$ is the Bessel function of the first kind. With our choice of the pump polarization, one third of the bonds participating in bimagnon excitation will be strongly altered, as illustrated in Fig. 3(d). Thereby, the resulting dynamically renormalized bimagnon energy is

$$\omega_{\text{bimag}}(A_0) \approx \omega_{\text{bimag}}(0) \left[\frac{2}{3} + \frac{1}{3} \sum_{m=-\infty}^{+\infty} \frac{\mathcal{J}_m(A_0)^2}{1 + m\Omega/U} \right]. \quad (11)$$

Figure 3(c) shows that the Floquet theory indeed can capture the softening of the bimagnon. On the other hand, since a finite-width pump contains all frequency components, it cannot be completely off-resonant. When the pump strength is strong enough, the Floquet theory prediction can deviate from the Raman calculation, as shown in Fig. 3(c). This deviation is more apparent at lower frequency ($\Omega = 10$ and $12t_h$) than at higher frequency ($\Omega = 16t_h$), since the former is closer to U .

When the pump frequency is on resonance, the magnon softening can be accompanied by other effects. At $\Omega = 8t_h = U$ shown in Fig. 3(b), the bimagnon first hardens instead of softens with increasing A_0 , and the energy also deviates from the Floquet prediction. Similar behaviors are also seen at $\Omega = 10t_h$ shown in Fig. 3(c). This deviation signals a coherent many-body renormalization due to the draining of electrons to unoccupied, real states. These occupancies typically enter through the corresponding energy and momentum positions of the Floquet virtual states, but become heavily renormalized by many-body scattering[45]. The selected occupied states then reversely correct the effective interaction and spin exchange energy.

In addition to energy shift, the bimagnon peak also broadens rapidly with increasing A_0 at high-frequency pumps. This broadening phenomenon is especially apparent under the resonance condition $\Omega \sim U$ [see for example Fig. 3(b)]. In the following we perform a quantitative analysis of the Stokes/anti-Stokes responses after the pump ($t = 10t_h^{-1}$) to show the clear distinction between on and off resonances. In fluctuation-dissipation theorem, the structure factor can be written as $\mathcal{R}(\omega) = \frac{1}{\pi} \text{Im}[\chi(\omega)] / (e^{-\omega/T} - 1)$. Since the imaginary part of the response $\chi(\omega)$ is an odd function, $\mathcal{R}(-\omega)/\mathcal{R}(\omega) = e^{-\omega/T}$. Therefore, an effective temperature can be defined as

$$T_{\text{eff}}(\omega) = \frac{\omega}{\ln \mathcal{R}(\omega) - \ln \mathcal{R}(-\omega)}. \quad (12)$$

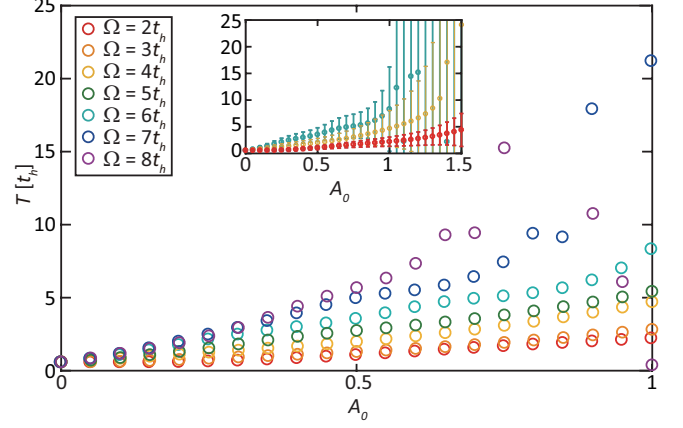


FIG. 4: Effective temperatures T_{eff} extracted from the post-pump ($t = 10t_h^{-1}$) ratio of Stokes/anti-Stokes responses averaged over energy range $4t_h < \omega < 12t_h$. The colors denote different pump frequencies Ω . The inset shows mean values and standard deviations of T_{eff} for $\Omega = 2, 4$ and $6t_h$.

Below we extract the effective temperatures T_{eff} averaged over energy range $4t_h < \omega < 12t_h$ for the Raman spectra at each time. An uncertainty associated with the standard deviation then can be defined for each T_{eff} . Within this procedure, T_{eff} remains nonzero even at $A_0 = 0$. This is because the fluctuation-dissipation theorem is exact only for spectra with zero linewidth. Therefore, our finite-width probe would give rise to a small error of $1/(\sqrt{2}\sigma_{\text{pr}}) = 0.3t_h$ in estimating T_{eff} .

Figure 4 shows that increasing Ω would enhance T_{eff} linearly at small A_0 , as the fluence is roughly proportional to ΩA_0^2 . However, at larger pump amplitudes $A_0 \gtrsim 1$, the uncertainty of T_{eff} can become comparable to its mean or even diverge [see the inset of Fig. 4]. This indicates that many-body renormalization becomes dominant over thermalization under high-frequency and large-amplitude pumps. Many-body scattering can significantly alter the wavefunction and lead to a nonequilibrium state violating the fluctuation-dissipation theorem. Reflected in the Raman spectra, it is the break down of extracting effective temperatures from the Stokes/anti-Stokes responses under strong pump pulse fields.

In summary, we have derived the theory of time-resolved Raman scattering and evaluated the B_{1g} Raman spectra on a pumped square-lattice single-band Hubbard model. The spectra were shown to exhibit different ultrafast processes, and each of them can become predominant under different pump conditions. In particular, thermalization dominates at small pump frequencies, and an effective temperature can be extracted. In contrast, for large-frequency “off-resonance” pumps, the Floquet theory successfully captures the renormalization of effective spin exchange interaction as manifested in the softening of the bimagnon energy. When the pump frequency is “on-resonance” to the Mott gap, coherent

many-body effects start to contribute. While thermalization still dominates at low pump fluences, many-body scattering takes over at large pump amplitudes and results in nonequilibrium states violating the Fermi-Dirac distribution. Time-resolved Raman scattering provides a platform for exploring the interplay between different ultrafast processes and opens up new opportunities to directly probe and manipulate spin exchange out of equilibrium. In accord with our theoretical predictions, detailed experimental investigations of the pump amplitude, frequency, and polarization would be intriguing future studies especially for strongly correlated systems.

Y.W. is supported by the Postdoctoral Fellowship in Quantum Science of the Harvard-MPQ Center for Quantum Optics. T.P.D. acknowledges support from the U.S. Department of Energy, Office of Science, Office of Basic Energy Sciences, Division of Materials Sciences and Engineering, under Contract No. DE-AC02-76SF00515. C.-C. C. is supported in part by the National Science Foundation under Grant No. OIA-1738698. This research used resources of the National Energy Research Scientific Computing Center (NERSC), a U.S. Department of Energy Office of Science User Facility operated under Contract No. DE-AC02-05CH11231.

-
- [1] J. Zhang and R. Averitt, *Annu. Rev. Mater. Res.* **44**, 19 (2014).
 - [2] D. Basov, R. Averitt, and D. Hsieh, *Nat. Mater.* **16**, 1077 (2017).
 - [3] C. C. Tsuei and J. R. Kirtley, *Rev. Mod. Phys.* **72**, 969 (2000).
 - [4] D. J. Scalapino, *Rev. Mod. Phys.* **84**, 1383 (2012).
 - [5] T. A. Maier, P. Staar, V. Mishra, U. Chatterjee, J. C. Campuzano, and D. J. Scalapino, *Nat. Commun.* **7**, 11875 (2016).
 - [6] Z. Meng, T. Lang, S. Wessel, F. Assaad, and A. Muramatsu, *Nature* **464**, 847 (2010).
 - [7] L. Balents, *Nature* **464**, 199 (2010).
 - [8] T. Chatterji, *Neutron scattering from magnetic materials* (Gulf Professional Publishing, 2005).
 - [9] S. Wolf, D. Awschalom, R. Buhrman, J. Daughton, S. Von Molnar, M. Roukes, A. Y. Chtchelkanova, and D. Treger, *Science* **294**, 1488 (2001).
 - [10] I. Žutić, J. Fabian, and S. D. Sarma, *Rev. Mod. Phys.* **76**, 323 (2004).
 - [11] D. Fausti, R. Tobey, N. Dean, S. Kaiser, A. Dienst, M. Hoffmann, S. Pyon, T. Takayama, H. Takagi, and A. Cavalleri, *Science* **331**, 189 (2011).
 - [12] M. Mitrano, A. Cantaluppi, D. Nicoletti, S. Kaiser, A. Perucchi, S. Lupi, P. Di Pietro, D. Pontiroli, M. Riccò, S. Clark, et al., *Nature* (2016).
 - [13] Y. Wang, C.-C. Chen, B. Moritz, and T. Devereaux, *Phys. Rev. Lett.* **120**, 246402 (2018).
 - [14] Y. Wang, C. Jia, B. Moritz, and T. P. Devereaux, *Phys. Rev. Lett.* **112**, 156402 (2014).
 - [15] J. Mentink, K. Balzer, and M. Eckstein, *Nat. Comm.* **6** (2015).
 - [16] M. Claassen, H.-C. Jiang, B. Moritz, and T. P. Devereaux, *Nat. Commun.* **8**, 1192 (2017).
 - [17] G. Batignani, D. Bossini, N. Di Palo, C. Ferrante, E. Pontecorvo, G. Cerullo, A. Kimel, and T. Scopigno, *IEEE J Quantum Electron.* **9**, 506 (2015).
 - [18] S. Sugai, S.-i. Shamoto, and M. Sato, *Phys. Rev. B* **38**, 6436 (1988).
 - [19] R. R. P. Singh, P. A. Fleury, K. B. Lyons, and P. E. Sulewski, *Phys. Rev. Lett.* **62**, 2736 (1989).
 - [20] T. P. Devereaux and R. Hackl, *Rev. Mod. Phys.* **79**, 175 (2007).
 - [21] C.-C. Chen, C. J. Jia, A. F. Kemper, R. R. P. Singh, and T. P. Devereaux, *Phys. Rev. Lett.* **106**, 067002 (2011).
 - [22] S. Ruhman, A. G. Joly, and K. A. Nelson, *IEEE J Quantum Electron.* **24**, 460 (1988).
 - [23] J. Chesnoy and A. Mokhtari, *Phys. Rev. A* **38**, 3566 (1988).
 - [24] A. M. Weiner, D. Leaird, G. P. Wiederrecht, and K. A. Nelson, *JOSA B* **8**, 1264 (1991).
 - [25] A. Kahan, O. Nahmias, N. Friedman, M. Sheves, and S. Ruhman, *J. Am. Chem. Soc.* **129**, 537 (2007).
 - [26] C. Schnedermann, V. Muders, D. Ehrenberg, R. Schlesinger, P. Kukura, and J. Heberle, *J. Am. Chem. Soc.* **138**, 4757 (2016).
 - [27] G. Batignani, E. Pontecorvo, G. Giovannetti, C. Ferrante, G. Fumero, and T. Scopigno, *Sci. Rep.* **6**, 18445 (2016).
 - [28] M. Jen, S. Lee, K. Jeon, S. Hussain, and Y. Pang, *The Journal of Physical Chemistry B* **121**, 4129 (2017).
 - [29] C. Ferrante, G. Batignani, G. Fumero, E. Pontecorvo, A. Virga, L. Montemiglio, G. Cerullo, M. Vos, and T. Scopigno, *J Raman Spectrosc.* **49**, 913 (2018).
 - [30] P. Bowlan, S. Trugman, D. Yarotski, A. Taylor, and R. Prasankumar, *J. Phys.D Appl. Phys.* **51**, 194003 (2018).
 - [31] Y. Wang, H. Steinberg, P. Jarillo-Herrero, and N. Gedik, *Science* **342**, 453 (2013).
 - [32] F. Mahmood, C.-K. Chan, Z. Alpichshev, D. Gardner, Y. Lee, P. A. Lee, and N. Gedik, *Nat. Phys.* (2016).
 - [33] A. P. Itin and M. I. Katsnelson, *Phys. Rev. Lett* **115**, 075301 (2015).
 - [34] L. D'Alessio and M. Rigol, *Phys. Rev. X* **4**, 041048 (2014).
 - [35] A. Lazarides, A. Das, and R. Moessner, *Phys. Rev. E* **90**, 012110 (2014).
 - [36] M. Bukov, M. Kolodrubetz, and A. Polkovnikov, *Phys. Rev. Lett.* **116**, 125301 (2016).
 - [37] L. D'Alessio and A. Polkovnikov, *Ann. Phys.* **333**, 19 (2013).
 - [38] P. Ponte, Z. Papić, F. Huveneers, and D. A. Abanin, *Phys. Rev.Lett.* **114**, 140401 (2015).
 - [39] A. Lazarides, A. Das, and R. Moessner, *Phys. Rev. Lett.* **115**, 030402 (2015).
 - [40] T. Kuwahara, T. Mori, and K. Saito, *Ann. Phys.* **367**, 96 (2016).
 - [41] T. Mori, T. Kuwahara, and K. Saito, *Phys. Rev. Lett.* **116**, 120401 (2016).
 - [42] D. A. Abanin, W. D. Roeck, and F. Huveneers, *Phys. Rev. Lett.* **115**, 256803 (2015).
 - [43] P. Werner, N. Tsuji, and M. Eckstein, *Phys. Rev. B* **86**, 205101 (2012).
 - [44] M. Moeckel and S. Kehrein, *Phys. Rev. Lett.* **100**, 175702 (2008).
 - [45] Y. Wang, M. Claassen, B. Moritz, and T. Devereaux,

- Phys. Rev. B **96**, 235142 (2017).
- [46] See Supplemental Material for the derivation of time-resolved Raman cross section, the cluster/polarization geometry, the spectral dependence on the interaction U , and the impact of different probe profiles.
 - [47] R. B. Lehoucq, D. C. Sorensen, and C. Yang, *ARPACK Users' Guide: Solution of Large-Scale Eigenvalue Problems with Implicitly Restarted Arnoldi Methods* (Siam, 1998).
 - [48] C. Jia, Y. Wang, C. Mendl, B. Moritz, and T. Devereaux, Comput. Phys. Commun. **224**, 81 (2018).
 - [49] S. R. Manmana, A. Muramatsu, and R. M. Noack, AIP Conf. Proc. **789**, 269 (2005).
 - [50] M. Balzer, N. Gdaniec, and M. Potthoff, J. Phys. Condens. Matter **24**, 035603 (2012).
 - [51] To reduce the impact of the elastic mode and better resolve the bimagnon peak, we perform the peak analysis for $R_{B_{1g}}(\omega, t) - R_{B_{1g}}(-\omega, t)$ instead.

Supplementary Material: Ultrafast Manipulation of Spin Dynamics in Time-Resolved Raman Scattering

Yao Wang,¹ T. P. Devereaux,^{2,3} and Cheng-Chien Chen⁴

¹*Department of Physics, Harvard University, Cambridge, Massachusetts 02138, USA*

²*SLAC National Accelerator Laboratory, Stanford Institute for Materials and Energy Sciences,
2575 Sand Hill Road, Menlo Park, California 94025, USA*

³*Geballe Laboratory for Advanced Materials, Stanford University, California 94305, USA*

⁴*Department of Physics, University of Alabama at Birmingham, Birmingham, Alabama 35294, USA*

(Dated: April 19, 2019)

I. THEORETICAL DERIVATION OF THE TIME-RESOLVED RAMAN FORMALISM

Equation (1) in the main text gives the probe Hamiltonian \mathcal{H}_{pr} in second-order perturbation of the probe field $\mathbf{A}^{(\text{pr})}$. In momentum space, the Hamiltonian reads

$$\mathcal{H}_{\text{pr}} = - \sum_{\mathbf{q}, \alpha} \hat{j}_{\alpha}(\mathbf{q}) A_{\alpha}^{(\text{pr})}(\mathbf{q}) - \frac{1}{2} \sum_{\substack{\mathbf{q}, \mathbf{q}_i \\ \alpha, \beta}} \hat{\gamma}_{\alpha\beta}(\mathbf{q}) A_{\alpha}^{(\text{pr})}(\mathbf{q}_s)^* A_{\beta}^{(\text{pr})}(\mathbf{q}_i) \quad (1)$$

In second quantization of the photon field, $A_{\alpha}^{(\text{pr})}(\mathbf{q}) = a_{\mathbf{q}\alpha} + a_{-\mathbf{q}\alpha}^{\dagger}$, and \mathcal{H}_{pr} can be rewritten as

$$\mathcal{H}_{\text{pr}} = \mathcal{H}_{\text{pr}}^{(\text{ab})} + \mathcal{H}_{\text{pr}}^{(\text{ab}2)} + \mathcal{H}_{\text{pr}}^{(\text{sc})} + h.c. \quad (2)$$

Here, the single-photon absorption part is $\mathcal{H}_{\text{pr}}^{(\text{ab})} = - \sum_{\mathbf{q}, \alpha} \hat{j}_{\alpha}(\mathbf{q}) a_{\mathbf{q}\alpha}$, the two-photon absorption part is $\mathcal{H}_{\text{pr}}^{(\text{ab}2)} = -\frac{1}{2} \sum_{\substack{\mathbf{q}, \mathbf{q}_i \\ \alpha, \beta}} \hat{\gamma}_{\alpha\beta}(\mathbf{q}) a_{-\mathbf{q}_s\alpha} a_{\mathbf{q}_i\beta}$, the scattering part is $\mathcal{H}_{\text{pr}}^{(\text{sc})} = -\frac{1}{2} \sum_{\substack{\mathbf{q}, \mathbf{q}_i \\ \alpha, \beta}} \hat{\gamma}_{\alpha\beta}(\mathbf{q}) a_{\mathbf{q}_s\alpha}^{\dagger} a_{\mathbf{q}_i\beta}$, and their Hermitian conjugates are written separately in Eq. (2). $\mathcal{H}_{\text{pr}}^{(\text{sc})}$ itself is Hermitian.

The unitary time propagator \mathcal{U} can be expanded in terms of the probe Hamiltonian \mathcal{H}_{pr} to second order:

$$\begin{aligned} \mathcal{U}(t, -\infty) &= \mathcal{T} e^{-i \int_{-\infty}^t [\mathcal{H}(\tau) + \mathcal{H}_{\text{pr}}(\tau)] d\tau} \\ &\approx \mathcal{T} e^{-i \int_{-\infty}^t \mathcal{H}(\tau) d\tau} - i \int_{-\infty}^t \mathcal{U}_0(t, \tau) \mathcal{H}_{\text{pr}}(\tau) \mathcal{U}_0(\tau, -\infty) d\tau \\ &\quad - i \int_{-\infty}^t dt_2 \int_{-\infty}^{t_2} dt_1 \mathcal{U}_0(t, t_2) \mathcal{H}_{\text{pr}}(t_2) \mathcal{U}_0(t_2, t_1) \mathcal{H}_{\text{pr}}(t_1) \mathcal{U}_0(t_1, -\infty) \\ &= \mathcal{T} e^{-i \int_{-\infty}^t \mathcal{H}(\tau) d\tau} - i \int_{-\infty}^t \mathcal{U}_0(t, \tau) \mathcal{H}_{\text{pr}}^{(\text{ab})}(\tau) \mathcal{U}_0(\tau, -\infty) d\tau - i \int_{-\infty}^t \mathcal{U}_0(t, \tau) \mathcal{H}_{\text{pr}}^{(\text{ab}2)}(\tau) \mathcal{U}_0(\tau, -\infty) d\tau \\ &\quad - i \int_{-\infty}^t dt_2 \int_{-\infty}^{t_2} dt_1 \mathcal{U}_0(t, t_2) \mathcal{H}_{\text{pr}}^{(\text{ab})}(t_2) \mathcal{U}_0(t_2, t_1) \mathcal{H}_{\text{pr}}^{(\text{ab})}(t_1) \mathcal{U}_0(t_1, -\infty) \\ &\quad - i \int_{-\infty}^t dt_2 \int_{-\infty}^{t_2} dt_1 \mathcal{U}_0(t, t_2) \mathcal{H}_{\text{pr}}^{(\text{ab})*}(t_2) \mathcal{U}_0(t_2, t_1) \mathcal{H}_{\text{pr}}^{(\text{ab})}(t_1) \mathcal{U}_0(t_1, -\infty) - i \int_{-\infty}^t \mathcal{U}_0(t, \tau) \mathcal{H}_{\text{pr}}^{(\text{sc})}(\tau) \mathcal{U}_0(\tau, -\infty) d\tau. \end{aligned} \quad (3)$$

Here we denote the unperturbed propagator $\mathcal{T} e^{-i \int_{t_1}^{t_2} \mathcal{H}(\tau) d\tau}$ as $\mathcal{U}_0(t_2, t_1)$. To simplify the notation, we represent $|\psi(t)\rangle$ as $|t\rangle$. Since the equilibrium ground state is usually selected as $|t = -\infty\rangle$, the Hermitian conjugate terms of $\mathcal{H}_{\text{pr}}^{(\text{ab})}$ and $\mathcal{H}_{\text{pr}}^{(\text{ab}2)}$ do not contribute to the first four integrals, as the ground state cannot emit any photon. The second term in Eq. (3) is the single-photon absorption related to linear optical conductivity. The third and fourth terms are the two-photon absorption reflected in nonlinear conductivity. The last two terms correspond to photon scattering.

The scattering amplitude and Raman intensity are related to $\mathcal{S}_{\mathbf{q}_i\mathbf{q}_s}^{\alpha\beta} = a_{\mathbf{q}_i\beta} a_{\mathbf{q}_i\alpha}^{\dagger}$ and $\mathcal{O}_{\mathbf{q}_i\mathbf{q}_s}^{\alpha\beta} = \mathcal{S}_{\mathbf{q}_i\mathbf{q}_s}^{\alpha\beta\dagger} \mathcal{S}_{\mathbf{q}_i\mathbf{q}_s}^{\alpha\beta}$, respectively.

The four-photon scattering operator selectively detects the last two integrals in Eq. (3) through the observable $\langle \mathcal{O} \rangle(t)$:

$$\begin{aligned}
\langle \mathcal{O} \rangle(t) = & \langle -\infty | \mathcal{U}_0(-\infty, t) \mathcal{O}_{\mathbf{q}_i \mathbf{q}_s}^{\alpha\beta} \mathcal{U}_0(t, -\infty) | -\infty \rangle \\
& + 4 \int_{-\infty}^t d\tau d\tau' \langle -\infty | \mathcal{U}_0(-\infty, \tau') \mathcal{H}_{\text{pr}}^{(\text{sc})\dagger}(\tau') \mathcal{U}_0(\tau', t) a_{\mathbf{q}_i \alpha} a_{\mathbf{q}_s \beta}^\dagger a_{\mathbf{q}_s \beta} a_{\mathbf{q}_i \alpha}^\dagger \mathcal{U}_0(t, \tau) \mathcal{H}_{\text{pr}}^{(\text{sc})}(\tau) \mathcal{U}_0(\tau, -\infty) | -\infty \rangle \\
& + 2 \text{Re} \int_{-\infty}^t d\tau dt_2' \int_{-\infty}^{t_2'} dt_1' \langle -\infty | \mathcal{U}_0(-\infty, t_1') \mathcal{H}_{\text{pr}}^{(\text{ab})\dagger}(t_1') \mathcal{U}_0(t_1', t_2') \mathcal{H}_{\text{pr}}^{(\text{ab})\dagger}(t_2') \mathcal{U}_0(t_2', t) a_{\mathbf{q}_i \alpha} a_{\mathbf{q}_s \beta}^\dagger a_{\mathbf{q}_s \beta} a_{\mathbf{q}_i \alpha}^\dagger \mathcal{U}_0(t, \tau) \\
& \mathcal{H}_{\text{pr}}^{(\text{sc})}(\tau) \mathcal{U}_0(\tau, -\infty) | -\infty \rangle + \int_{-\infty}^t dt_2 dt_2' \int_{-\infty}^{t_2'} dt_1' \int_{-\infty}^{t_2} dt_1 \langle -\infty | \mathcal{U}_0(-\infty, t_1') \mathcal{H}_{\text{pr}}^{(\text{ab})\dagger}(t_1') \mathcal{U}_0(t_1', t_2') \mathcal{H}_{\text{pr}}^{(\text{ab})}(t_2') \\
& \mathcal{U}_0(t_2', t) a_{\mathbf{q}_i \alpha} a_{\mathbf{q}_s \beta}^\dagger a_{\mathbf{q}_s \beta} a_{\mathbf{q}_i \alpha}^\dagger \mathcal{U}_0(t, t_2) \mathcal{H}_{\text{pr}}^{(\text{ab})\dagger}(t_2) \mathcal{U}_0(t_2, t_1) \mathcal{H}_{\text{pr}}^{(\text{ab})}(t_1) \mathcal{U}_0(t_1, -\infty) | -\infty \rangle.
\end{aligned} \tag{4}$$

The first term contributes only to elastic scattering. The last term involving intermediate states between t_1 and t_2 is related to “resonant” scattering. In contrast, the second and third terms are associated with “non-resonant” and “mixed” scatterings, respectively. When the incoming photon frequency ω_i is off-resonance to any excited state, the last two terms in Eq. (4) can be ignored. Moreover, in the optical limit $\mathbf{q} = \mathbf{q}_i - \mathbf{q}_s \approx 0$, the odd parity of $\hat{j}_\alpha(0)$ forbids any finite resonant contribution. Without resonant intermediate states, the absolute energies of incoming and outgoing photons are irrelevant. Only the energy difference $\omega = \omega_i - \omega_s$ is important for non-resonant scattering. Therefore, the optical, non-resonant time-resolved Raman cross section with explicit polarizations can be written as

$$R_{\alpha\beta}(\omega, t) = 4 \int_{-\infty}^{\infty} d\tau d\tau' \langle -\infty | \mathcal{U}_0(-\infty, \tau') \mathcal{H}_{\text{pr}}^{(\text{sc})\dagger}(\tau') \mathcal{U}_0(\tau', \infty) a_{\mathbf{q}_i \alpha} a_{\mathbf{q}_s \beta}^\dagger a_{\mathbf{q}_s \beta} a_{\mathbf{q}_i \alpha}^\dagger \mathcal{U}_0(\infty, \tau) \mathcal{H}_{\text{pr}}^{(\text{sc})}(\tau) \mathcal{U}_0(\tau, -\infty) | -\infty \rangle \tag{5}$$

As detectors collect signals over a time period much longer than the probe pulse width, the integral limit can be set to $+\infty$. Here t in $R_{\alpha\beta}(\omega, t)$ indicates the center of the probe. Using Wick’s theorem, Eq. (5) can be simplified to

$$R_{\alpha\beta}(\omega, t) = \int_{-\infty}^{\infty} dt_1 dt_2 s_{\mathbf{q}_i}(\infty, \tau')^* s_{\mathbf{q}_s}(\infty, \tau') s_{\mathbf{q}_s}(\infty, \tau) s_{\mathbf{q}_i}(\infty, \tau) \chi_{\alpha\beta}(t_1, t_2), \tag{6}$$

where the response function $\chi_{\alpha\beta}(t_1, t_2) = i \langle t_2 | \hat{\gamma}_{\alpha\beta}(t_2) \mathcal{U}_0(t_2, t_1) \hat{\gamma}_{\alpha\beta}(t_1) | t_1 \rangle$ and $s_{\mathbf{q}}(t_2, t_1) = \langle t_2 | a_{\mathbf{q}}^\dagger \mathcal{U}_0(t_2, t_1) a_{\mathbf{q}} | t_1 \rangle \approx \sqrt{[n_{\mathbf{q}}^{\text{ph}}(t_2) + 1] n_{\mathbf{q}}^{\text{ph}}(t_1)} e^{-i\omega_{\mathbf{q}}(t_1 - t_2)}$. In the semiclassical limit, the photon annihilation operator gives the square root of the instantaneous photon number. In the finite probe width limit $t_2 \rightarrow \infty$, $n_{\mathbf{q}}^{\text{ph}}(t_2) = 0$, so the photon part contributes to an instantaneous shape function with a phase factor $s_{\mathbf{q}_s}(\infty, \tau)^* s_{\mathbf{q}_i}(\infty, \tau) \approx g(\tau; t) e^{-i\omega\tau}$. Therefore,

$$R_{\alpha\beta}(\omega, t) = \int_{-\infty}^{\infty} dt_1 dt_2 e^{i\omega(t_2 - t_1)} g(t_1; t) g(t_2; t) \chi_{\alpha\beta}(t_1, t_2). \tag{7}$$

On square lattice, the polarization can be decomposed as irreducible representation of D_{4h} point group in the long-wavelength limit, and thereby the above equation produces Eqs. (6) and (7) in the main text. As the probe is treated above as a perturbation, in the main text we omit the subscripts of $\chi_{\alpha\beta}$ and unify it with the propagator as $\mathcal{U}(t_2, t_1)$. For the shape function, we consider a typical gaussian probe pulse field $g(t'; t) = 1/(\sqrt{2\pi}\sigma_{\text{pr}}) e^{-(t' - t)^2/2\sigma_{\text{pr}}^2}$.

Finally, we note that in equilibrium, the system is time-translationally invariant: $\chi_{\alpha\beta}(t_1, t_2) = \chi_{\alpha\beta}(t_2 - t_1)$. Then

$$\begin{aligned}
R_{\alpha\beta}(\omega, t) &= \frac{1}{2\pi\sigma_{\text{pr}}^2} \int_{-\infty}^{\infty} dt_1 dt_2 e^{i\omega(t_2 - t_1)} e^{-(t_1 - t)^2/2\sigma_{\text{pr}}^2} e^{-(t_2 - t)^2/2\sigma_{\text{pr}}^2} \chi_{\alpha\beta}(t_2 - t_1) \\
&= \frac{1}{2\pi\sigma_{\text{pr}}^2} \int_{-\infty}^{\infty} dT d\tau e^{i\omega\tau} e^{-(T - t)^2/\sigma_{\text{pr}}^2} e^{-\tau^2/4\sigma_{\text{pr}}^2} \chi_{\alpha\beta}(\tau) \\
&= \frac{\sigma_{\text{pr}}^2}{\pi} \int_{-\infty}^{\infty} d\omega' e^{-(\omega' - \omega)^2\sigma_{\text{pr}}^2} \mathcal{R}_{\alpha\beta}(\omega'),
\end{aligned} \tag{8}$$

which thereby reproduces the equilibrium, time-independent Raman cross section with a linewidth $\sim 1/(\sqrt{2}\sigma_{\text{pr}})$.

II. POLARIZATION DEPENDENCE

In the main text, we consider the horizontal pump polarization $\mathbf{e}_{\text{pol}} = \mathbf{e}_x$. As shown in Fig. S1, this direction corresponds to the diagonal direction in momentum space, due to the tilted geometry of the 12A Betts cluster.

Changing the polarization direction from horizontal $\mathbf{e}_{\text{pol}} = \mathbf{e}_x$ to a tilted polarization (corresponding to the horizontal momentum-space direction) would result in a projection along both basis vectors. With such a projection, the renormalization of the spin exchange energy is less obvious, as shown in Fig. S2(b). This is because the horizontal direction in momentum space is less nested, and the pump field does not help much cross-gap excitations. Therefore, the related thermalization effect is also less obvious.

III. U DEPENDENCE

Figure S3 examines the time-resolved B_{1g} Raman spectra for two different strengths of Hubbard U . As the spin exchange energy is roughly $J = 4t_h^2/U$, the bimagnon energy for $U = 8t_h$ is smaller than that for $U = 6t_h$, while the charge gap is larger in the former by definition. Here we consider a pump frequency $\Omega = 6t_h$, which should be on resonance to certain excited states in both situations. Due to the expected strong thermalization and many-body effects, we select a relatively weak pump strength $A_0 = 0.3$. As shown in Fig. S3, the bimagnon softening is more obvious for $U = 6t_h$, since the electron is more delocalized compared to that for $U = 8t_h$. In general, the $U = 6t_h$ system is more venerable to the same pump condition, with greater bimagnon softening, more obvious anti-Stokes features, and stronger spectral redistribution inside the charge gap. A more delocalized system also makes the calculations more sensitive to the small-cluster size/geometry and causes a stronger equilibrium elastic peak.

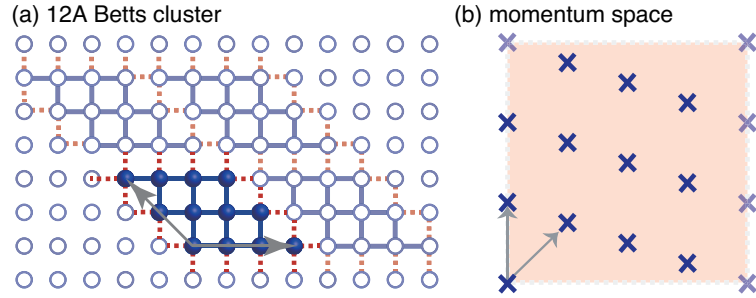


FIG. S1: The 12A Betts cluster in (a) real space and (b) momentum space. The gray arrows denote basis vectors. The solid and dotted lines in (a) represent respectively the intra- and inter-cluster hopping terms.

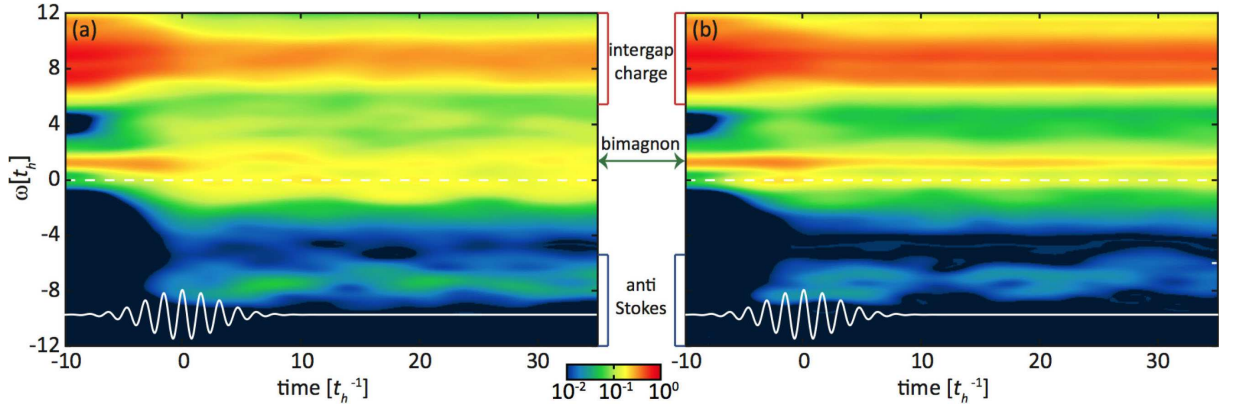


FIG. S2: Time-resolved B_{1g} Raman spectra with pump amplitude $A_0 = 0.6$ and frequency $\Omega = 4t_h$ for (a) horizontal polarization $\mathbf{e}_{\text{pol}} = \mathbf{e}_x$ [same as Fig. 2 in the main text] and (b) tilted polarization corresponding to the horizontal momentum space. The dashed white line denotes the Fermi level, and the solid white curve shows the pump profile. The excitations are marked in the middle.

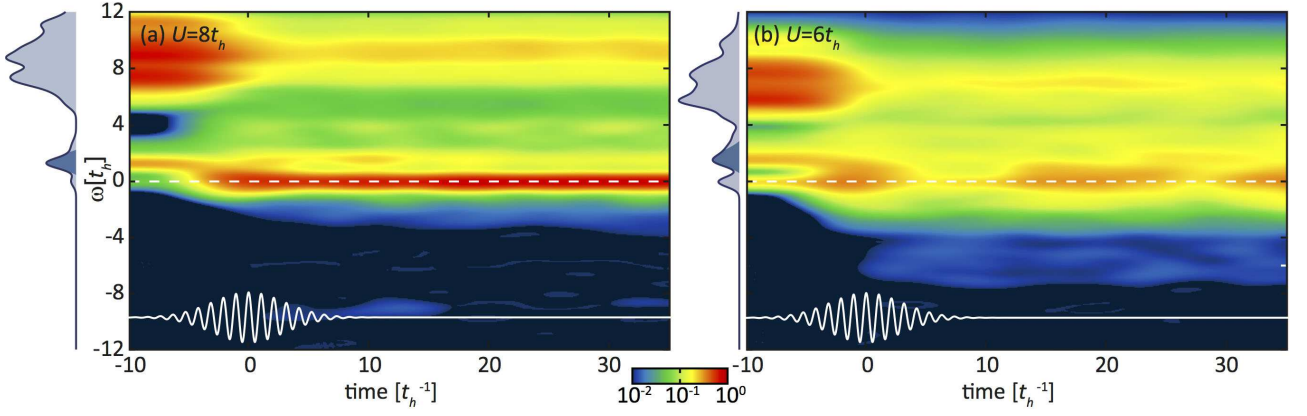


FIG. S3: Time-resolved B_{1g} Raman spectra with $A_0 = 0.3$ and $\Omega = 6t_h$ for (a) $U = 8t_h$ and (b) $U = 6t_h$. The horizontal polarization $\mathbf{e}_{\text{pol}} = \mathbf{e}_x$ is considered. The plots are drawn in the same manner as Fig. S2. The shaded curves on the left of each panel show the corresponding equilibrium B_{1g} Raman spectra. The bimagnon peak is denoted by a darker color.

IV. IMPACT OF THE PROBE WIDTH

While the pump profile changes the dynamics of the three ultrafast processes discussed in the main text, the probe profile determines only the spectral resolution in both frequency and time domain, without changing the underlying physics. Figure S4 shows the time-resolved B_{1g} spectra probed by different pulse widths $\sigma_{\text{pr}} = 4t_h^{-1}$ and $\sigma_{\text{pr}} = 6t_h^{-1}$. The same pump profile as that in Figs. 2 and S2 (which have $\sigma_{\text{pr}} = 2t_h^{-1}$) is used. Due to the uncertainty principle, a wider probe has less time but more energy/frequency resolutions, which is reflected already in the equilibrium spectra. The finer frequency structure with wider probe width in Fig. S4 shows that the bimagnon peak is a sharp, well-defined quasiparticle. In addition, the continuum of excitation above the charge gap consists of many poles, which now can be more easily resolved with a wider probe. Figure S4 shows clearly that both thermalization and Floquet renormalization happen during the pump. After the pump, a wider probe also clearly resolves the softening and broadening of the bimagnon peak. On the other hand, with the gain in frequency resolution, the price to pay for a wider probe is a bad time resolution. For example, unlike the oscillatory features observable in Figs. S2(a) and S4(a), the $\sigma_{\text{pr}} = 6t_h^{-1}$ spectrum in Fig. S4(b) exhibits almost a constant structure in time after the pump. This constant structure is essentially the time average of that in a narrower probe.

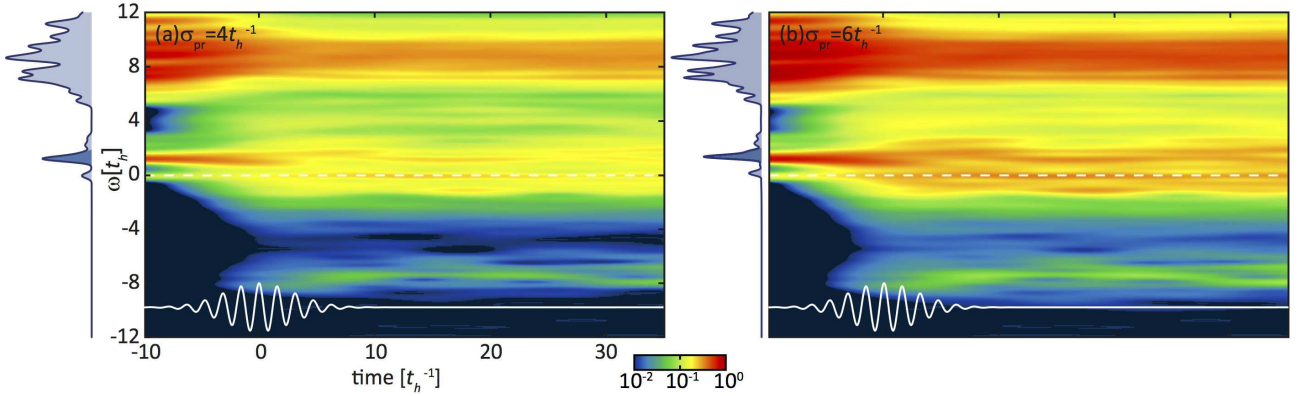


FIG. S4: Time-resolved B_{1g} Raman spectra with probe pulse width (a) $\sigma_{\text{pr}} = 4t_h^{-1}$ and (b) $\sigma_{\text{pr}} = 6t_h^{-1}$. The plots are drawn in the same manner as Fig. S2. The pump profile is identical to that in Fig. 2 in the main text. The shaded curves on the left of each panel show the corresponding equilibrium B_{1g} Raman spectra. The bimagnon peak is denoted by a darker color.